

Three-Dimensional Simulation of Eccentric LWD Tool Response in Boreholes Through Dipping Formations

Yik-Kiong Hue, Fernando L. Teixeira, *Senior Member, IEEE*, Luis San Martin, and Michael S. Bittar

Abstract—We simulate the response of logging-while-drilling (LWD) tools in complex three-dimensional (3-D) borehole environments using a finite-difference time-domain (FDTD) scheme in cylindrical coordinates. Several techniques are applied to the FDTD algorithm to improve the computational efficiency and the modeling accuracy of more arbitrary geometries/media in well-logging problems: 1) a 3-D FDTD cylindrical grid to avoid staircasing discretization errors in the transmitter, receiver, and mandrel geometries; 2) an anisotropic-medium (unsplit) perfectly matched layer (PML) absorbing boundary condition in cylindrical coordinates is applied to the FDTD algorithm, leading to more compact grids and reduced memory requirements; a simple and efficient algorithm is employed to extract frequency-domain data (phase and amplitude) from early-time FDTD data; 4) permittivity scaling is applied to overcome the Courant limit of FDTD and allow faster simulations of lower frequency tool; and 5) two locally conformal FDTD (LC-FDTD) techniques are applied to better simulate the response of logging tools in eccentric boreholes. We validate the FDTD results against the numerical mode matching method for problems where the latter is applicable, and against pseudoanalytical results for eccentric borehole problems. The comparisons show very good agreement. Results from 3-D borehole problems involving eccentric tools and dipping beds simultaneously are also included to demonstrate the robustness of the method.

Index Terms—Borehole problem, finite-difference time-domain (FDTD) method, logging-while-drilling (LWD) tool, oil exploration, well-logging.

I. INTRODUCTION

NUMERICAL simulation of electromagnetic well-logging tools in complex borehole environments is of great importance for the interpretation of measurement data and characterization of oil reservoirs [1]–[3]. Numerical methods such as finite-element [4] (FEM), finite-difference frequency-domain (FDFD) [5], and transmission line matrix (TLM) methods [3], as well as pseudoanalytical methods such as numerical mode matching [6] (NMM) and conjugate gradient fast Fourier-Hankel transform (CG-FFHT) type methods [7], have been employed in the past to study the electromagnetic response of well-logging tools. Numerical methods such as FEM

and FDFD discretize Maxwell's equations directly, and hence can be applied to study general tool geometries and responses in arbitrary three-dimensional (3-D) formations. However, such (frequency-domain) methods require the solution of a large sparse linear system. This can become impractical in current machines for large 3-D well-logging problems, especially when the number of unknowns grows beyond 10^6 – 10^7 . Moreover, the presence of large resistivity contrasts, which is common in many geophysical formations, poses an additional challenge for both FEM and FDFD methods because the associated linear system can become ill-posed. The NMM and CG-FFHT, on the other hand, are much faster and efficient methods but cannot be easily applied to arbitrary tool geometries and 3-D formations.

In this paper, we discuss the implementation and use of finite-difference time-domain (FDTD) methods for the modeling of well-logging tools. Similarly to FEM and FDFD, the FDTD method can solve for arbitrary 3-D formations, since it discretizes Maxwell's equations directly. However, FDTD involves an explicit time-domain update method. As a result, FDTD does not require the solution of a linear system (matrix-free), and larger problems can be solved. Indeed, FDTD can be classified as an optimal method in the sense that it exhibits $O(N)$ computational complexity per time step and requires $O(N)$ memory, where N is the number of unknowns. The drawback is that, since it requires a time stepping process, the FDTD solution can be slower for small problems than FEM and FD solutions in the frequency domain. Here, we discuss the application of several techniques to the standard FDTD algorithm to solve the well-logging problem more efficiently and accurately as follows.

- We implement the FDTD in a 3-D cylindrical grid to avoid staircasing discretization errors in the transmitter, receiver, and mandrel geometries.
- An anisotropic-medium (unsplit) perfectly matched layer (PML) absorbing boundary condition in cylindrical coordinates is applied to the FDTD algorithm, leading to more compact grids and reduced memory requirements for a problem of given (physical) size.
- A simple and efficient algorithm is applied to extract frequency domain data from early-time FDTD data, allowing phase and amplitude data to be obtained in shorter simulation times.
- For low-frequency problems, a scaling on permittivity values is applied to overcome the Courant limit and allow for larger time step sizes (and hence shorter simulation times).

Manuscript received October 19, 2003; revised September 15, 2004. This work was supported in part by Halliburton Energy Services, in part by the National Science Foundation under Grant ECS-0347502, and in part by the Ohio Supercomputer Center (OSC) under Grants PAS-0061 and PAS-0110.

Y.-K. Hue and F. L. Teixeira are with the ElectroScience Laboratory and Department of Electrical and Computer Engineering The Ohio State University, Columbus, OH 43212 USA (e-mail: hue.2@osu.edu, teixeira@ece.osu.edu).

L. S. Martin and M. S. Bittar are with the Sensor Physics Group, Halliburton Energy Services, Houston, TX 77032 USA (e-mail: luis.sanmartin@halliburton.com).

Digital Object Identifier 10.1109/TGRS.2004.841354

- In order to examine the effect of eccentricity on the tool response, two locally conformal FDTD (LC-FDTD) schemes are applied to model nonconformal borehole/formation interfaces.

The paper is organized as follows. In Section II, we discuss aspects of the FDTD formulation for the well-logging problem. In Section III, we describe in more detail the particular logging-while-drilling (LWD) tool geometry under consideration and its discretization using a cylindrical FDTD grid. In Section IV, we validate the FDTD results against NMM results and illustrate various applications of the algorithm to borehole problems involving eccentric tools, dipping bed formations, and/or high contrast between mud/formation conductivities. Finally, in Section V, we present some final remarks and draw the main conclusions.

II. FORMULATION

The use of a cylindrical FDTD algorithm instead of traditional Cartesian FDTD is advantageous for well-logging tools because it automatically conforms to the (cylindrical) tool geometry (mandrel, drill collar, and antennas) thus avoiding stair-casing errors caused by discretization. The use of a fully 3-D algorithm is important to study arbitrary formations, not restricted to axisymmetric geometries.

The spatial discretization adopted for the cylindrical FDTD here utilizes a staggered cylindrical grid [8], [9]. The cell size is uniform in the longitudinal z and azimuthal ϕ directions. In the radial ρ direction, nonuniform discretization is utilized to reduce overall memory requirements. Details on the spatial discretization are given in Section III.

A. Application of PML Absorbing Boundary Condition to 3-D Cylindrical FDTD Grids

In order to implement the FDTD algorithm for open-domain problems, an absorbing boundary condition is needed to truncate the computational domain and avoid spurious reflections from the computational boundaries. The 3-D anisotropic-medium cylindrical PML introduced in [9] is applied here for this purpose. Unlike the split-field PML formulation [8], [10], [11], the anisotropic-medium PML does not require modifications on Maxwell's equations. Instead, only the constitutive relations inside the PML region are modified. In cylindrical coordinates, the PML constitutive parameters (permittivity and permeability) are characterized by diagonal tensors $\bar{\epsilon}$, $\bar{\mu}$ given by [9]

$$\bar{\epsilon}_{\text{PML}} = \epsilon \bar{\Lambda}_{[\rho, \phi, z]}(\rho, z; \omega) \quad (1)$$

$$\bar{\mu}_{\text{PML}} = \mu \bar{\Lambda}_{[\rho, \phi, z]}(\rho, z; \omega) \quad (2)$$

with

$$\bar{\Lambda}_{[\rho, \phi, z]}(\rho, z; \omega) = \hat{\rho} \hat{\rho} \frac{\tilde{\rho} s_z}{\rho s_\rho} + \hat{\phi} \hat{\phi} \frac{\rho s_z s_\rho}{\tilde{\rho}} + \hat{z} \hat{z} \frac{\tilde{\rho} s_\rho}{\rho s_z}. \quad (3)$$

Here, $\tilde{\rho}$ is the analytic continuation of coordinate ρ to a complex variable domain, and s_ρ , s_z are frequency-dependent complex stretching variables [11], defined as

$$s_\rho(\rho) = a_\rho(\rho) + i \frac{\Omega_\rho(\rho)}{\omega} \quad (4)$$

$$s_z(z) = a_z(z) + i \frac{\Omega_z(z)}{\omega} \quad (5)$$

$$\begin{aligned} \tilde{\rho} &= \int_0^\rho s_\rho(\rho') d\rho' = \int_0^\rho \left(a_\rho(\rho') + i \frac{\Omega_\rho(\rho')}{\omega} \right) d\rho' \\ &= b_\rho(\rho) + i \frac{\Delta_\rho(\rho)}{\omega} \end{aligned} \quad (6)$$

where $a_\rho(\rho)$, $a_z(z)$ (real stretching parameter) and $\Omega_\rho(\rho)$, $\Omega_z(z)$ (PML conductivity) are functions of position only. The purpose of these variables is to change the eigenfunctions of the problem inside the PML [9] so as to produce reflectionless absorption. By choosing the $\Omega_{\rho, z} > 0$ propagating eigenfunctions of Maxwell's equations are mapped into exponentially decaying eigenfunctions inside the PML. Moreover, by letting $a_{\rho, z} > 1$, faster decay of evanescent modes are induced inside the PML. Both of these variables are chosen to gradually increase along the normal coordinate following a polynomial profile inside the PML. Inside the physical domain, $\Omega_{\rho, z} = 0$, and $a_{\rho, z} = 1$, so that the original equations are recovered. The optimal values and polynomial profile for $\Omega_{\rho, z}$ and $a_{\rho, z}$ are problem-dependent. In general, the best choice depends on the spatial discretization size, the number of cell used for the PML, the frequency spectrum of the excitation, and both the conductivity and permeability of the background medium. It is not our objective here to perform a detailed study on the optimal choices for these parameters.

B. Application of Locally Conformal FDTD for Eccentric Borehole Problems

Because of mechanical vibrations and/or gravitational pull effects, electromagnetic well-logging tools are not always perfectly aligned with the borehole axis. This leads to so-called *eccentricity* effects [12]. These are particularly prevalent in highly deviated drilling where the gravitational pull is more intense.

In the cylindrical FDTD, we choose the mandrel and antenna geometries to be conformal to the grid. As a result, eccentric tools produce borehole/formation interfaces that are not conformal to the cylindrical grid. Here, we model these interfaces by locally conformal (LC) FDTD algorithms. These algorithms have been previously explored to model curved dielectric interfaces in Cartesian grids [13]. In this section, we describe the application of the LC-FDTD approaches to the conductive borehole wall interfaces in the 3-D cylindrical grid.

1) *Edge-Based LC-FDTD*: The edge-based LC-FDTD approach utilizes an arithmetic mean over *edges* to derive effective permittivities $\epsilon_x^{\text{eff}}(i, j, k)$ and $\epsilon_y^{\text{eff}}(i, j, k)$. For conductive interfaces, effective conductivities can be obtained in an analogous manner.

Fig. 1 illustrates this approach. The curved interface crosses the edges $E_x(i, j, k)$ and $E_y(i, j, k)$. The conductivity used to update the associated fields is replaced by the effective one given by

$$\sigma_x^{\text{eff}}(i, j, k) = \frac{(\Delta x_2(i, j, k)\sigma_2 + (\Delta x - \Delta x_2(i, j, k))\sigma_1)}{\Delta x(i, j, k)} \quad (7)$$

$$\sigma_y^{\text{eff}}(i, j, k) = \frac{(\Delta y_2(i, j, k)\sigma_2 + (\Delta y - \Delta y_2(i, j, k))\sigma_1)}{\Delta y(i, j, k)} \quad (8)$$

respectively (linear weighting). Since the curved interface does not penetrate the remaining edges $E_x(i, j+1, k)$ and $E_y(i+1, j, k)$, the conductivity used to update the remaining field components is simply the corresponding conductivity of

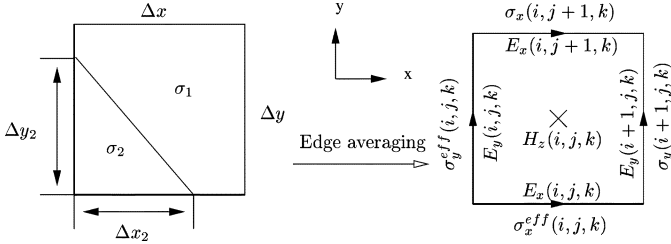


Fig. 1. Averaging procedure used in the edge-based conformal FDTD scheme showing, on the top, the intersection between the regular FDTD mesh and curved interface between two conductive media. (Left) The original problem with different conductivities along a single edge. (Right) The equivalent problem with effective conductivities along each edge.

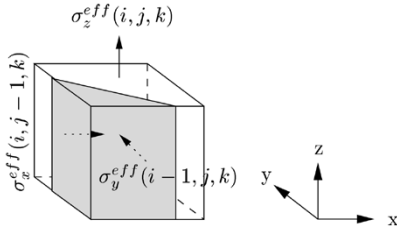


Fig. 2. Linear weighted averaging procedure used in the face-based conformal dielectric FDTD scheme. (Top) Three intersection between a curved interface and the FDTD *dual-grid* mesh. (Bottom) The equivalent problem using effective conductivities over each dual-grid face.

the region where the associated edge is situated. This modification can be incorporated with a minimal amount of extra bookkeeping in the cylindrical FDTD algorithm by identifying the edges intersected by the curved borehole/formation interface, and changing the corresponding conductivities by effective ones. In Section II-B.2, we discuss the application of face-based LC-FDTD for this same problem. The face-based LC-FDTD is more intuitively more appealing and indeed leads to more accurate results than edge-based LC-FDTD. We nevertheless include some edge-based results in the examples that follow, since this approach is still used in the FDTD literature.

2) *Face-Based LC-FDTD*: The second LC-FDTD approach utilizes *face-based* averaging. In this approach, a weighted mean is again used to obtain effective conductivities but the averaging process is now applied to the fields normal to the *dual-grid face* where the curved interface exists. Both the permittivity and conductivity are associated with a particular electric field, so when a material interface crosses the surface of a dual-grid cell, the permittivity and conductivity is weighted accordingly.

Fig. 2 illustrates this second approach. From Maxwell's equations in the integral form applied at a given dual-grid cell face, we have

$$\iint_S \left(\epsilon \frac{\partial \vec{E}}{\partial t} + \sigma \vec{E} \right) \cdot d\vec{S} = \iint_S \nabla \times \vec{H} \cdot d\vec{S} = \oint_l \vec{H} \cdot d\vec{l}. \quad (9)$$

Assuming constant electric field over each dual-grid cell face of the FDTD grid, the above equation simplifies to

$$(S_1 + S_2) \epsilon \frac{\partial \vec{E}}{\partial t} + (\sigma_1 S_1 + \sigma_2 S_2) \vec{E} = \oint_l \vec{H} \cdot d\vec{l}. \quad (10)$$

Here, S_1 and S_2 represent the partial areas of each dual-grid cell face corresponding to conductivities σ_1 and σ_2 , respectively

(gray and white areas in Fig. 2). The effective conductivity σ^{eff} then becomes the weighted average below

$$\sigma^{eff} = \frac{\sigma_1 S_1 + \sigma_2 S_2}{S_1 + S_2}. \quad (11)$$

Note that this approach applies to all three electric field components. The effective conductivities used in the FDTD update equations for each electric field component use the S_1 and S_2 calculated on the corresponding normal (dual-grid) face.

C. Application of Frequency Data Extraction Techniques for Treated FDTD Excitations

Well-logging problems usually involves CW (single frequency) operation (CW tools). For problems where the steady-state, CW behavior of the fields is of interest, it may be very costly to run the time-domain simulation for long periods of time to extract frequency-domain data, particularly for explicit time-domain methods, such as FDTD, in large 3-D domains. As a result, it is important to develop techniques to extract accurate frequency data at early times during the simulation.

To achieve this, we employ here a treatment on the time-domain source excitation and use the so-called two-equation two-unknown (2E2U) algorithm proposed in [14] for time-to-frequency conversion. The 2E2U is a very simple approach based on the solution of two linear equations in single-frequency analysis. Assuming a sinusoidal excitation at the source, one can approximate the field components at any location in the computational domain in the generic form

$$\begin{aligned} A \sin(\omega t_1 + \theta) &= q_1 \\ A \sin(\omega t_2 + \theta) &= q_2 \end{aligned} \quad (12)$$

where A and θ are the amplitude and the phase, and $\omega = 2\pi f$ is the angular frequency. These equations are an approximation because, in practice, one cannot have a pure sinusoidal excitation but only a truncated one due to the turn-on effect of the sources at $t = 0$. The turn-on effect produces high-frequency contamination and a dc offset as discussed later on. Given any two time instants t_1 and t_2 and corresponding field values q_1 and q_2 from the FDTD simulation, the unknowns A and θ can be obtained as

$$\begin{aligned} \theta &= \arctan \left[\frac{q_2 \sin(\omega t_1) - q_1 \sin(\omega t_2)}{q_1 \cos(\omega t_2) - q_2 \cos(\omega t_1)} \right] \\ A &= \left| \frac{q_1}{\sin(\omega t_1 + \theta)} \right|. \end{aligned} \quad (13)$$

Successive t_1 and t_2 are used during the FDTD update until convergence is reached for A and θ . In practice, t_1 and t_2 should be chosen sufficiently apart to avoid ill-conditioning when solving for A and θ . In practice, a satisfactory rule of thumb is to choose the absolute time difference between t_1 and t_2 to be around one tenth of the period $T = 1/f$.

Because of the turn-on effect at $t = 0$, the early excitation of the truncated sinusoidal source needs to be modified; otherwise, high-frequency contamination and dc offset [15] (i.e., a $1/t$ slowly decaying time-average signal) will occur, leading to a slower convergence in the frequency data extraction. A smooth turn-on of the (pseudo)sinusoidal source can be used to avoid such dc offset. In addition, a smooth turn-on avoids high-

frequency contamination from the discontinuity on the derivative at $t = 0$. In our case, we choose a time-domain excitation of the form $v_s(t) = r(t) \sin(\omega t)$, where $r(t)$ is a raised cosine (RC) ramp function given by

$$r(t) = \begin{cases} 0, & t < 0 \\ 0.5 \left[1 - \cos\left(\frac{\omega t}{2\alpha}\right) \right], & 0 \leq t \leq \alpha T \\ 1, & t > \alpha T \end{cases} \quad (14)$$

where $T = 2\pi/\omega$ is the period of the sine function, and α is the number of sine wave cycles during the ramp duration αT .

This particular excitation has the desirable properties that both the function and its first derivative are continuous for all values of α at $t = 0$. However, the dc offset is zero only for values of α multiples of 0.5.

Fig. 5 illustrates a typical convergence result for the phase difference between the LWD receivers using a ramp-sinusoidal function with $\alpha = 0.5$ and the 2E2U approach. The phase difference in this particular example converges after a time period approximately equals to $1.1T$.

D. Application of Permittivity Scaling for Lower Frequency Problems

In the FDTD algorithm, the Courant stability condition in a medium with μ , ϵ , and σ establishes an upper bound on the time step Δt_c given by [16]

$$\Delta t_c = v^{-1} \left[(\Delta \rho_{\min})^{-2} + (\rho_{\min} \Delta \phi)^{-2} + (\Delta z_{\min})^{-2} \right]^{-1/2} \quad (15)$$

where v is the phase velocity given by

$$v = (\epsilon \mu)^{-1/2}. \quad (16)$$

In well-logging problems, the spatial discretization resolution is often dictated by the smallest skin depth inside the conductive formation and not by the wavelength (since the former is often smaller than the latter). As a result, the maximum time step Δt_c can become very small compared to the period of the wave. A small Δt_c implies that the total number of time steps necessary to achieve convergence can become very large. This is especially true for low-frequency tools in high-conductivity formations.

Under these conditions, however, the displacement current is much smaller than the conduction current. When this occurs (diffusion dominated regime), one can simply scale up the permittivity ϵ of the medium to increase the maximum allowed time step [17], as can be seen by writing Maxwell's equations in frequency domain

$$\begin{aligned} \nabla \times \vec{E} - i\omega \mu \vec{H} &= 0 \\ \nabla \times \vec{H} - (\sigma - i\omega \epsilon) \vec{E} &= \vec{J}_s. \end{aligned} \quad (17)$$

Here, all field quantities are now complex phasors, and \vec{J}_s is the current excitation.

If $\sigma \gg \omega \epsilon$, the above simplifies to

$$\begin{aligned} \nabla \times \vec{E} - i\omega \mu \vec{H} &= 0 \\ \nabla \times \vec{H} - \sigma \vec{E} &= \vec{J}_s \end{aligned} \quad (18)$$

which does not depend on ϵ anymore. Hence, by scaling up ϵ (while still satisfying $\sigma \gg \omega \epsilon$), the Courant condition is relaxed without altering the physics of the problem. Permittivity scaling was also used in [18] to solve a diffusive time-domain problem.

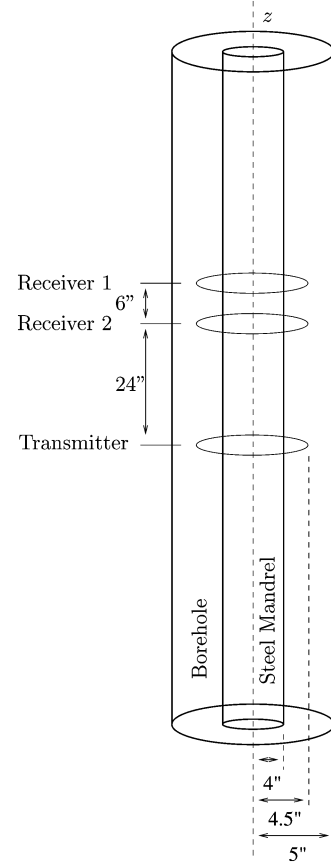


Fig. 3. Basic configuration of the LWD tool inside a 5-in-radius borehole.

In the present case, the only necessary postprocessing in the final results is the scaling back of field amplitudes to incorporate the change on the intrinsic impedance. This scaling will depend on the way the excitation is introduced in the problem. If an electric source is used, then a scaling up is effected on the magnetic field. For a magnetic source, a scaling down is effected on the electric field.

III. FDTD MODELING OF LWD TOOLS

The LWD tool configuration used here is illustrated in Fig. 3. The frequencies of operation in the examples considered range from 100 kHz to 2 MHz. The tool has a 8-in diameter steel mandrel at its center. The transmitter and receiver antennas consist of 4.5-in radius circular wire loops wrapped around the mandrel. To simulate these loop antennas in the FDTD grid, a spatial discretization employing either a gap source excitation or a continuous source excitation can be utilized. In the gap source excitation, a voltage source is impressed between two points (gap) of the wire transmitter antenna by enforcing the electric field to assume predetermined values along FDTD edges on a straight line between these two points. In the continuous source excitation, an electric current source is impressed throughout the FDTD nodes comprising the wire transmitter antennas by enforcing the magnetic field to assume predetermined values over small loops (Ampere's law) enclosing each FDTD node along the wire antenna. In the simulations that follow, we utilize continuous source excitations. The two single-loop receiver antennas are situated at 30 and 24 in away from a single-loop

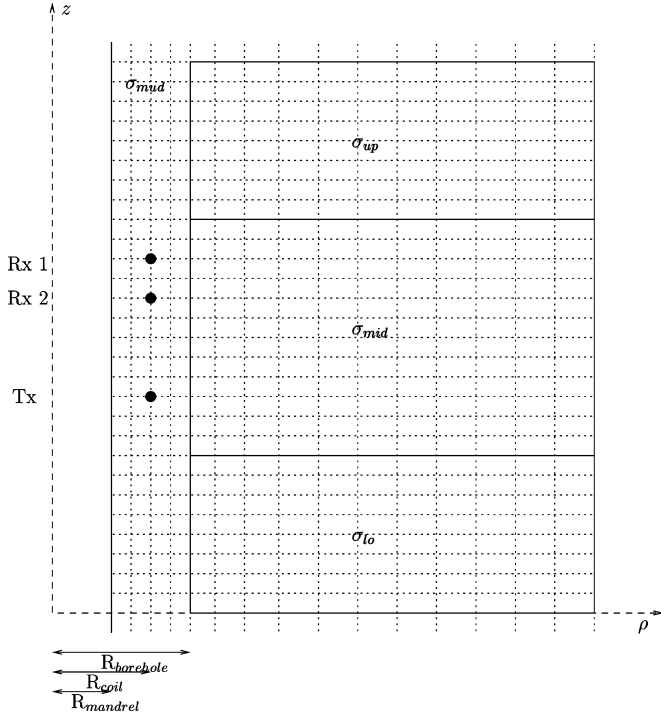


Fig. 4. Illustration of the cross-section of the LWD tool discretization in a layered formation.

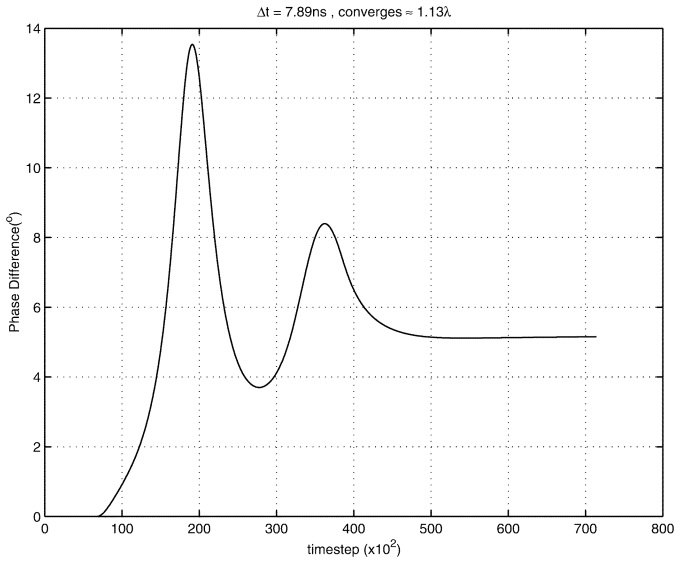


Fig. 5. Example of the convergence behavior of the phase difference between LWD tool receiver voltages using the 2E2U approach.

transmitter antenna. The quantities of interest are the phase difference (PD) and the amplitude ratio (AR) between the voltages measured at the two receiver antennas

$$\begin{aligned} PD &= \theta_{r2} - \theta_{r1} \\ AR &= \frac{A_{r2}}{A_{r1}} \end{aligned} \quad (19)$$

where θ and A is the phase and amplitude of the receiver voltages, and the subscripts $r1$ and $r2$ denote receiver 1 and 2, respectively.

A $\rho - z$ cross-section plane of the LWD tool discretization is depicted in Fig. 4. The discretization is nonuniform in the ρ

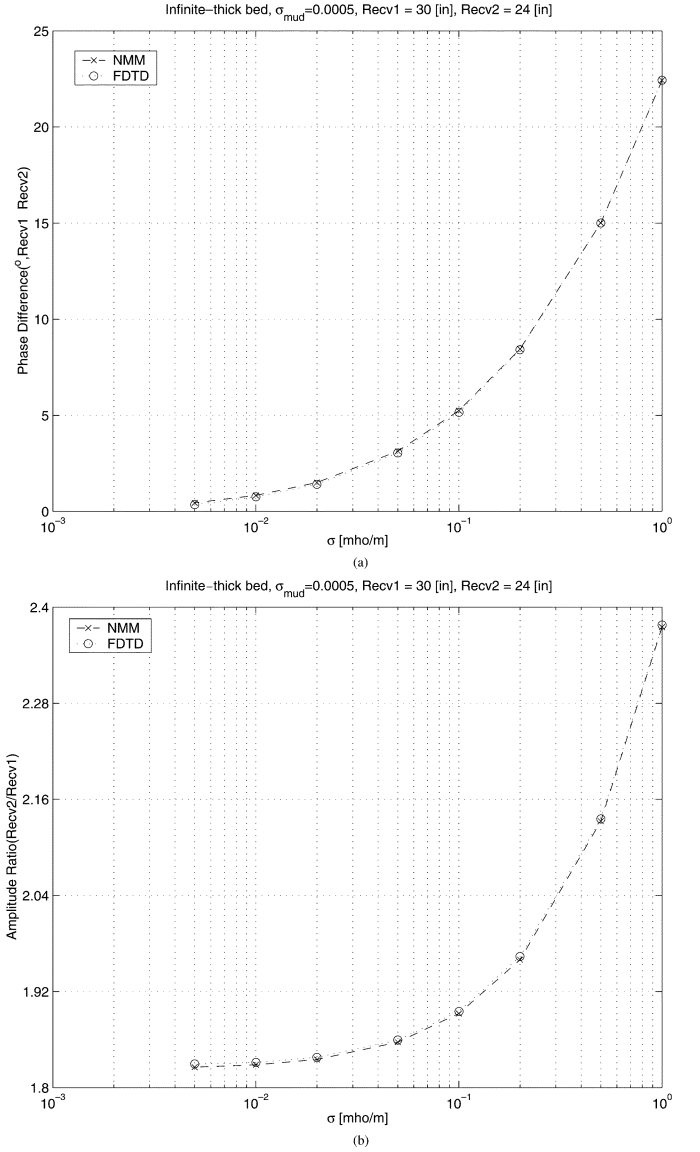


Fig. 6. FDTD and NMM results for phase difference (PD) and amplitude ratio (AR) of a LWD tool in a uniform formation (infinitely thick bed) for various values of formation conductivities. The mud conductivity is fixed at 0.0005 mho/m.

direction, and includes two cells between the coils. Outside the coils, $\Delta\rho$ is gradually increased to minimize memory requirements. The maximum cell size is chosen as $(\Delta\rho)_{\max} = \delta/5$ where δ is the skin depth corresponding to the largest conductivity value in the formation. The increase in $\Delta\rho$ is gradual to avoid spurious reflections due to abrupt changes in the discrete impedance of the grid (which depends on the local cell size). The skin depth is given as

$$\delta = \frac{1}{\omega\sqrt{\mu\epsilon}} \left\{ \frac{1}{2} \left[\sqrt{1 + \left(\frac{\sigma}{\omega\epsilon}\right)^2} - 1 \right] \right\}^{-1/2} \text{ m.} \quad (20)$$

For $(\sigma/(\omega\epsilon)) \gg 1$, this reduces to

$$\delta = \sqrt{\frac{2}{\omega\mu\sigma}}. \quad (21)$$

A uniform discretization is employed along both the longitudinal z and azimuthal ϕ directions.

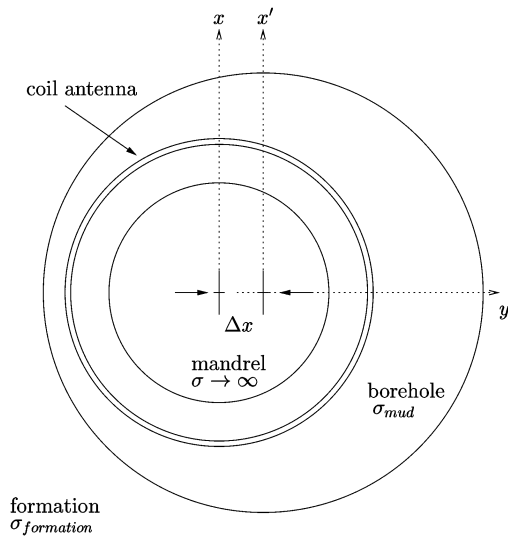


Fig. 7. Horizontal cross-section of an eccentric borehole problem.

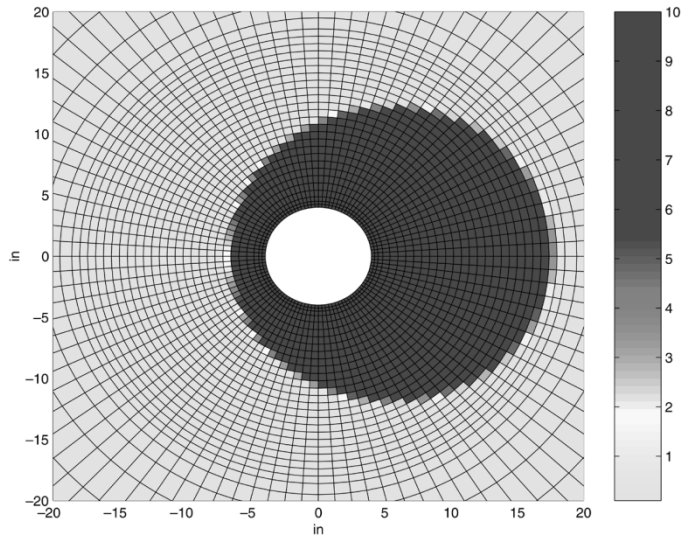


Fig. 8. Conductivity distribution along the horizontal cross-section of the cylindrical FDTD for an eccentric LWD tool scenario.

IV. RESULTS

A. Homogeneous Formations

Fig. 6 depicts the phase difference response of the LWD tool in a borehole surrounded by homogeneous formations (infinitely thick bed) with different conductivities. The tool operates at 2 MHz, and the borehole has 10-in diameter in this case. The conductivity of the mud (borehole fluid) is equal to 5×10^{-4} mho/m (oil-based mud). A two-dimensional (2-D) version of the algorithm can be employed in this case, since the problem is axisymmetric. The domain is discretized using a $(N_\rho, N_z) = (50, 180)$ grid. The PML is set up using ten cells both in ρ and z directions and a cubic taper profile for both the real and imaginary parts of the stretching variables. The cell discretization size in the longitudinal direction in $\Delta z = 3.81$ cm, while in the radial direction $\Delta \rho$ varies from 0.635 cm close to the mandrel to 3.18 cm at the outer edges.

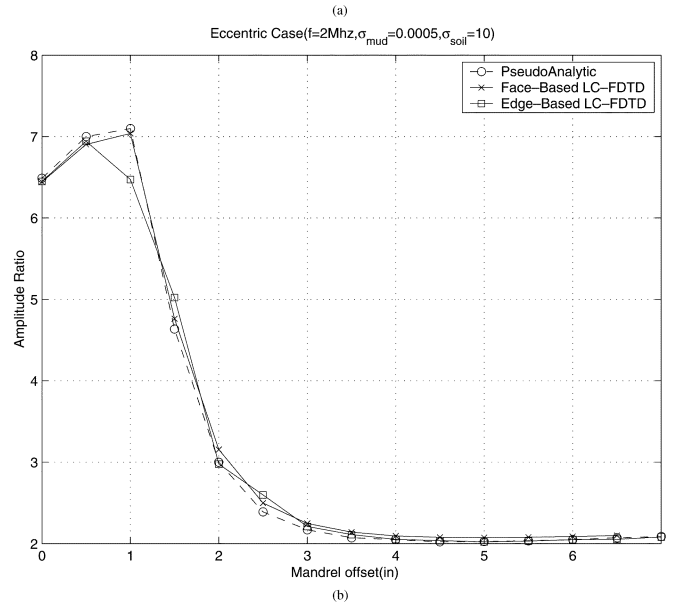
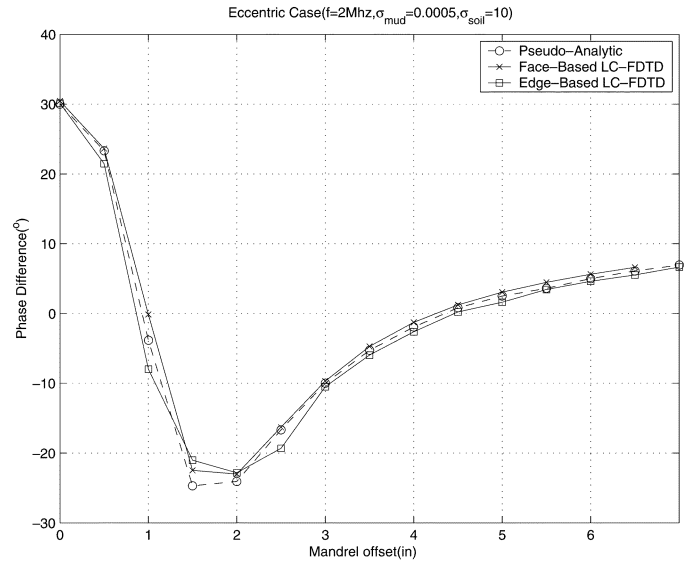


Fig. 9. FDTD simulation results versus pseudoanalytical results of eccentric LWD tool responses. Phase difference and amplitude ratio are plotted against the mandrel offset Δx (see Fig. 7). The borehole has 12-in radius and is filled with oil-based mud $\sigma = 0.0005$ mho/m. The surrounding homogeneous formation has $\sigma = 10$ mho/m. Very good agreement is observed between the FDTD and pseudoanalytical results.

This latter value is determined according to the skin depth of the formation with largest conductivity. The results are compared against NMM results in Fig. 6, showing very good agreement for all conductivity values.

B. Eccentric Tools

We next simulate an eccentric borehole problem, where the LWD tool is not aligned with the borehole axis, as illustrated in Fig. 7. The conductivity distribution over an horizontal cross-section (xy plane) of the 3-D FDTD grid is depicted in Fig. 8, where face-based averaging of the borehole and formation conductivities are visible at the borehole/formation interface.

Fig. 9 shows results from the simulation of an LWD tool in a mud with $\sigma = 0.0005$ mho/m) and 12-in radius borehole.

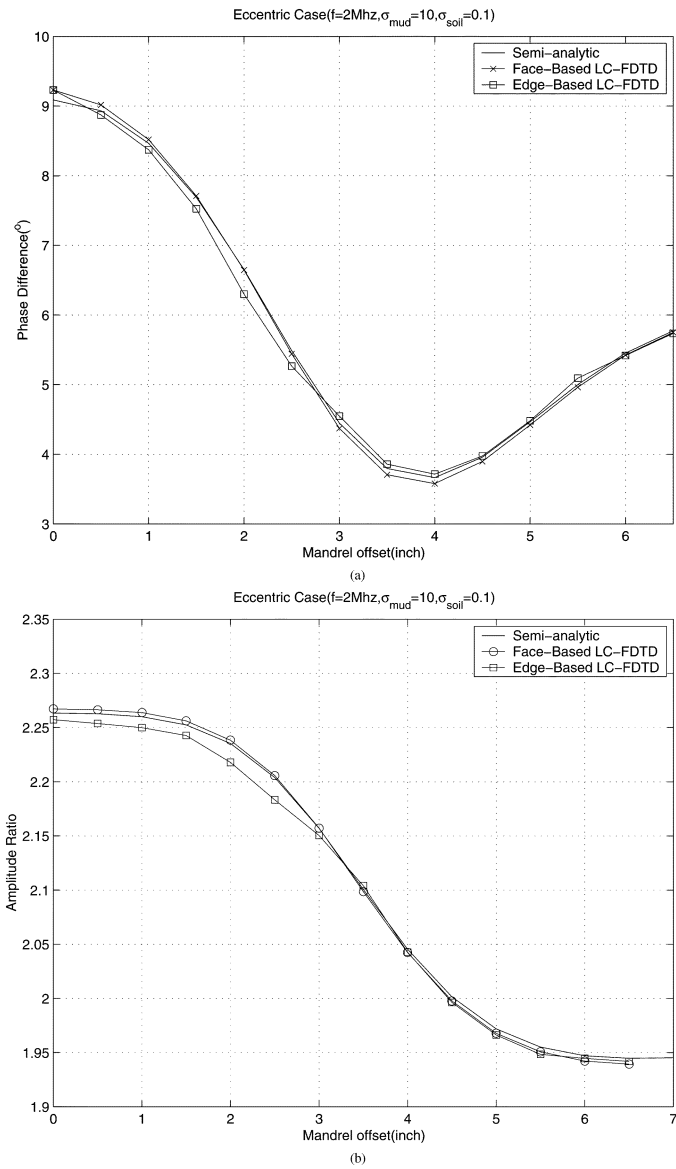


Fig. 10. FfDTD simulation results versus pseudoanalytical results of eccentric LWD tool responses. Phase difference and amplitude ratio are plotted against the mandrel offset Δx (see Fig. 7). The borehole has 12-in radius and is filled with oil-based mud $\sigma = 10.0$ mho/m. The surrounding homogeneous formation has $\sigma = 0.1$ mho/m. Very good agreement is again observed between the FDTD and pseudoanalytical results.

The abscissa in this figure represents the mandrel offset, i.e., the distance between the mandrel axis and the borehole axis, as indicated in Fig. 7. The tool operates at 2 MHz. The formation is homogenous with $\sigma = 10$ mho/m, and different eccentricities are considered. The discretization of the domain in this case utilizes a $(N_\rho, N_\phi, N_z) = (50, 76, 430)$ grid. The PML has ten cells with cubic taper profiles in both the ρ and z directions. The discretization is nonuniform in ρ direction, with $\Delta\rho$ varying from 0.635–18.77 cm, and uniform in z direction, with $\Delta z = 1.524$ cm. Fig. 9 compares the face-based and edge-based LC-FDTD against pseudoanalytical results, showing very good agreement. Face-based LC-FDTD consistently perform slightly better than the edge-based LC-FDTD.

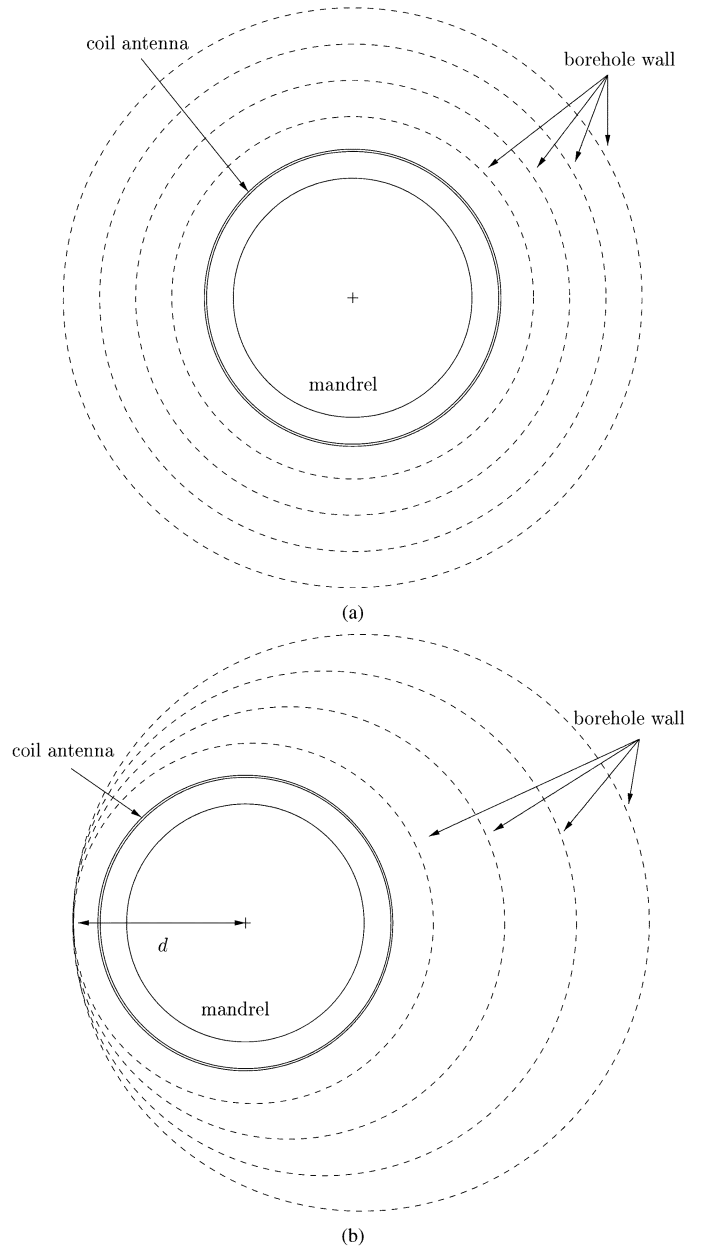


Fig. 11. Influence of eccentricity and borehole size on LWD tool response. (a) Case 1: Borehole size is varied while keeping mandrel centered. (b) Case 2: Borehole size is varied while keeping the offset distance Δx fixed.

In general, the effect of eccentricity on the tool response is larger when the conductivity contrast between the mud and the surrounding formation is high. To illustrate this point, Fig. 10 shows results for the same 2-MHz LWD in a 12-in borehole now with water-based mud with $\sigma = 10$ mho/m) in homogeneous formation with $\sigma = 0.1$ mho/m. The discretization utilizes the same parameters as the previous example. The variation on the (absolute) phase difference and amplitude ratio as a function of the eccentricity is clearly less pronounced in this case. Face-based and edge-based LC-FDTD again show very good agreement against pseudoanalytical results.

The maximum degree of eccentricity depends on the ratio between the borehole and mandrel radii. In other words, for a given

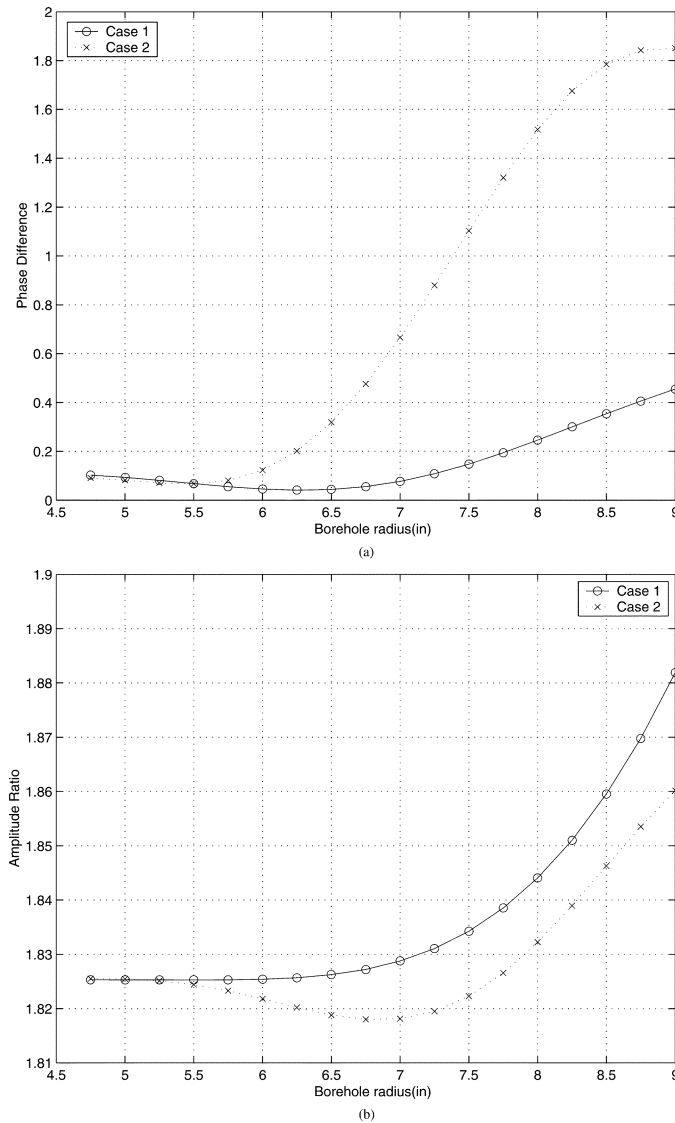


Fig. 12. FDTD simulation of the response of eccentric LWD tools in a homogenous formation. A high-contrast case is considered with mud and formation conductivities equal to 10 and 0.0001 mho/m, respectively. Case 1 curve is the LWD tool response versus borehole radius while the tool is kept at the center of the borehole [see Fig. 11(a)]. Case 2 curve is the LWD tool response versus borehole size while keeping a fixed distance $d = 4.75$ in from the mandrel axis to closest borehole wall [see Fig. 11(b)].

tool geometry (mandrel radius), the maximum variation on the tool response due to eccentricity effects can be established as a function of the borehole radius. To illustrate the latter point, we consider two borehole scenarios. In the first scenario, we let the borehole size vary while keeping the logging tool centered (Case 1), as illustrated in Fig. 11(a). In the second scenario, we let the borehole size vary while keeping the distance from the logging tool to the borehole wall fixed (Case 2) and equal to $\Delta x = 4.75$ in, as illustrated in Fig. 11(b). We consider a high-contrast case where the conductivity of the mud is $\sigma = 10$ mho/m and the conductivity of the formation is $\sigma = 0.0001$ mho/m. The phase difference and amplitude ratio between the receiver voltages is plotted against the borehole radius in Fig. 12. The difference between Case 1 and Case 2 is

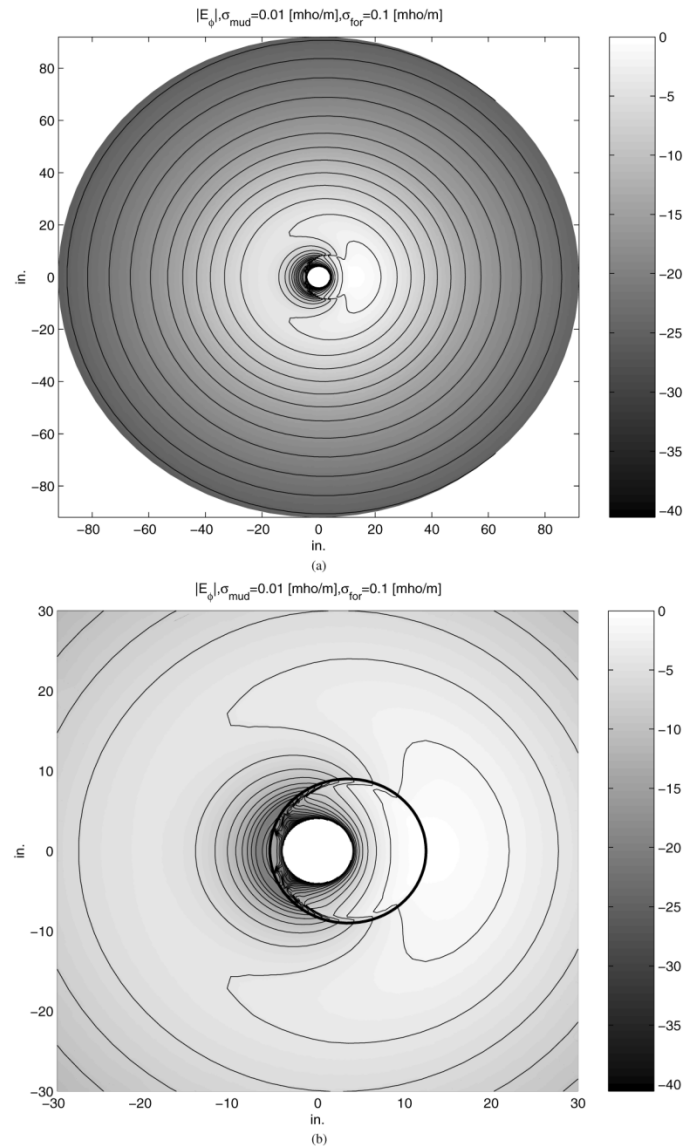


Fig. 13. Electric field (ϕ component) distribution on the horizontal cross-section of the cylindrical FDTD grid for an eccentric LWD tool. (Top) An expanded view of the field distribution on the formation. (Bottom) Zoomed view of the field distribution close to the borehole. The mud conductivity is $\sigma_{\text{mud}} = 0.01$ mho/m, and the formation conductivity is $\sigma_{\text{for}} = 0.1$ mho/m.

produced solely by the eccentricity effect. These two curves provides us with a range of values for phase difference and amplitude ratio in a borehole of given size when the degree of eccentricity is not exactly known (as often occurs in practice). From this figure, we observe that the variation of the tool response due to eccentricity effects is more limited for smaller size boreholes, as expected.

To illustrate qualitatively the effect of the eccentricity on the field distribution, we plot in Figs. 13 and 14 the ϕ component electric field distribution along the horizontal cross section of the borehole. In this case, the mandrel axis is situated 3.5 in away from the borehole axis in a borehole with 9-in radius. In Fig. 13, the conductivity of the mud and formation are $\sigma_{\text{mud}} = 0.01$ and $\sigma_{\text{for}} = 0.1$, respectively. In Fig. 14, the conductivity

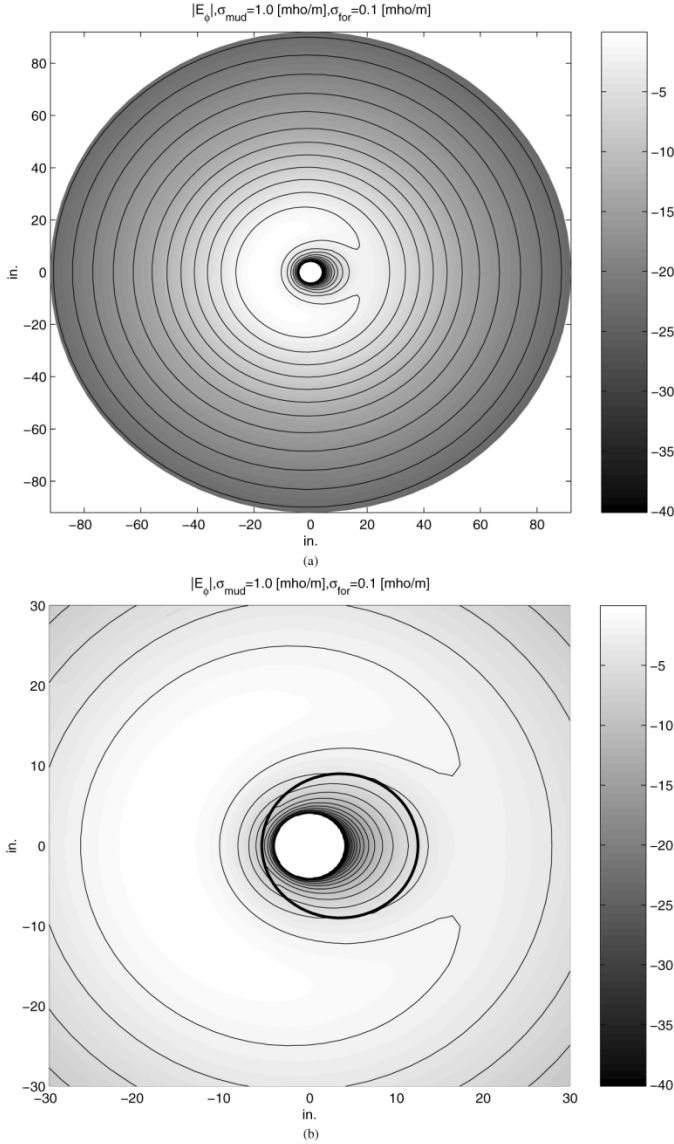


Fig. 14. Electric field (ϕ component) distribution on the horizontal cross-section of the cylindrical FDTD grid for an eccentric LWD tool. (Top) An expanded view of the field distribution on the formation. (Bottom) Zoomed view of the field distribution close to the borehole. The mud conductivity is again $\sigma_{\text{mud}} = 1.0$ mho/m, and the formation conductivity is now $\sigma_{\text{for}} = 0.1$ mho/m in this case.

of the mud and formation are $\sigma_{\text{mud}} = 1.0$ and $\sigma_{\text{for}} = 0.1$, respectively. In these figures, we observe that the field penetrates asymmetrically into the formation due to eccentricity effect. The field penetration profile not only depends on the degree of eccentricity but also on the relative conductivities of the mud and the surrounding formation.

C. Eccentric Tools in Dipping Beds

The present FDTD method allows the simulation of LWD tool problems in eccentric and dipping bed environments simultaneously. Fig. 15 shows the simulation results for an LWD tool operating at 2 MHz on a three-layer formation with dipping bed for various eccentricities and dipping angles. The middle layer (dipping bed) is 60 in thick. The upper and

lower layers have conductivity $\sigma = 1$ mho/m, whereas the middle layer has conductivity $\sigma = 0.01$ mho/m. The borehole has 9-in radius. We consider an oil-based mud with $\sigma = 0.0005$ mho/m.

The discretization employs a $(N_\rho, N_\phi, N_z) = (50, 60, 175)$ grid. The PML has ten cells with cubic taper profiles in both the ρ and z directions. The discretization is nonuniform in ρ direction, with $\Delta\rho$ varying from 0.635–7.11 cm, and uniform in z direction, with $\Delta z = 5.08$ cm. We use the face-based LC-FDTD to model the eccentric geometry and a staircasing approximation to model the dipping bed. The ECCE label in Fig. 15 represents the offset distance Δx (in inches) of the eccentric tool as indicated in Fig. 7. Compared to [19] and [20], the noneccentric results in these figures show very similar behavior according to the dip angle.

From these plots, we can observe two main effects caused by the eccentricity. First, as mentioned before, the change on the apparent resistivity due to the eccentricity effect is larger when the contrast between the mud and the resistivity (conductivity) of the surrounding layer is larger. Note that, in this example, the larger contrast occurs in the upper and lower layers (leftmost and rightmost regions of the figure, respectively). In addition, the eccentricity produces an increase in the horn effect in the highly deviated bed case for this example.

D. LWD Tools at Lower Frequencies

Fig. 16 shows the simulation results for a LWD tool operating at 500 kHz, using a water-based mud with $\sigma = 2$ mho/m in a three-layer formation where the center bed is again 60 in thick. The FDTD results are validated against NMM results showing very good agreement. This problem is axisymmetric and the discretization of the 2-D domain in this case uses a $(N_\rho, N_z) = (50, 130)$ grid. Since the skin depth is larger at this lower frequency, the cell size in the ρ direction varies from 0.635–14.24 cm. Note that, for lower frequencies, large variations on the cell size have less impact on the discrete impedance because the number of grid points per wavelength is much larger. The z direction cell size is uniformly discretized with $\Delta z = 7.62$ cm. The PML is inserted over the ten outermost cells in along the radial direction and over the bottom ten and top ten cells along the longitudinal z direction. The PML employs a cubic tapered profile on both the real and imaginary part of the stretching variables.

Next, we simulate the same tool operating at 100 kHz. The discretization in this case employs a $(N_\rho, N_z) = (40, 200)$ grid. The discretization cell is nonuniform in the ρ direction varying from 0.635–31.83 cm, and uniform in the z direction with $\Delta z = 7.62$ cm. The ten-layer PML employs a cubic tapered profile only in the *real* part of the stretching variables. No imaginary stretching is used, since this is now an essentially diffusive problem. Permittivity scaling is desirable at this frequency because the ratio of the displacement current to the conduction current is very small, $(\omega\epsilon/\sigma) \approx 5.56 \times 10^{-4}$. A time step much larger than established by the Courant condition 15 can then be used, as illustrated in Table I. Fig. 17 shows a comparison between FDTD and NMM results for

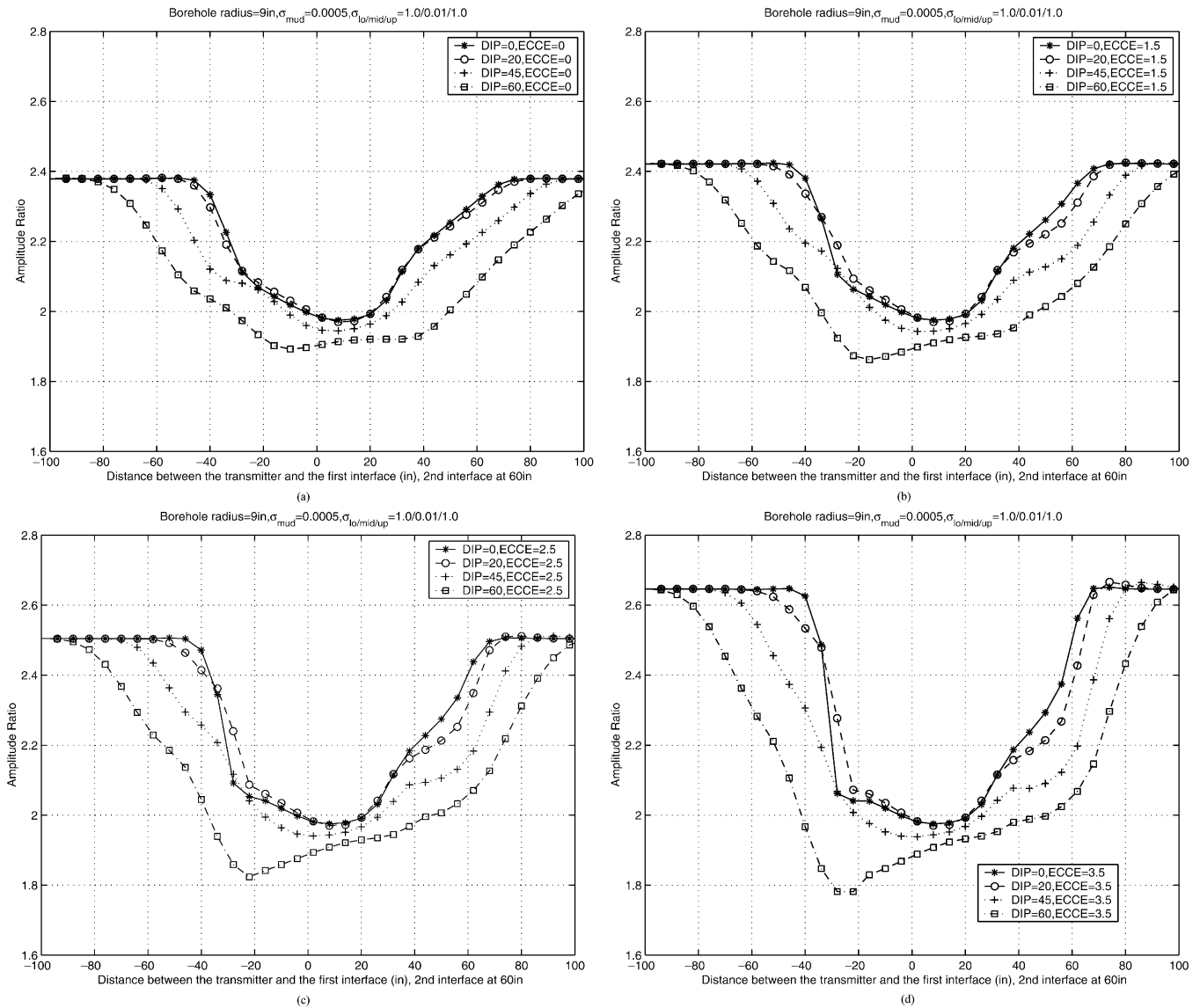


Fig. 15. FDTD simulations of eccentric LWD tools in formations with dipping beds. The upper and lower layer conductivities is $\sigma = 1$ mho/m, while the 60-in-thick dipping bed has $\sigma = 0.01$. The borehole has radius 9 in and is filled with oil-based mud with $\sigma = 0.0005$. The label ECCE in this plots represents the offset distance Δx in inches (see Fig. 7).

the phase difference and amplitude ratio in this case. FDTD results use $\epsilon_r = 1, 17.975$, and 179.75 . This figure shows that the scaled permittivity results still provide very accurate results. The phase velocity, wavelength, time step, and normalized CPU time for $\epsilon_r = 1, 17.975$, and 179.75 are given in Table I.

V. CONCLUSION

We have described the application of several techniques to model eccentric borehole problems in dipping formations using cylindrical FDTD. Results from FDTD simulations were validated against pseudoanalytical and NMM results (when the latter are applicable) in a number of scenarios, including eccentric tools with high-conductivity contrast between mud and formation and for varying degrees of eccentricity.

For the examples considered, the effect of eccentricity on the tool response is observed to be more important when the conductivity contrast between the mud and the surrounding formation is high, as expected. The specific behavior of the amplitude ratio and phase difference versus the degree of eccentricity depends on the particular mud and formation conductivities involved, as illustrated in Figs. 9 and 10. When considered together with deviated formations, it was observed that eccentric geometries can produce an increase in the horn effect for large dipping angles, as shown in Fig. 15.

The maximum degree of eccentricity in a borehole problem is a function of the ratio between the mandrel and borehole radii. For a given ratio, curves indicating the predicted variations on the tools response caused to eccentricity effects can be obtained by simulating the responses of both centered (axisymmetric) and maximally eccentric cases, such as provided in Fig. 12.

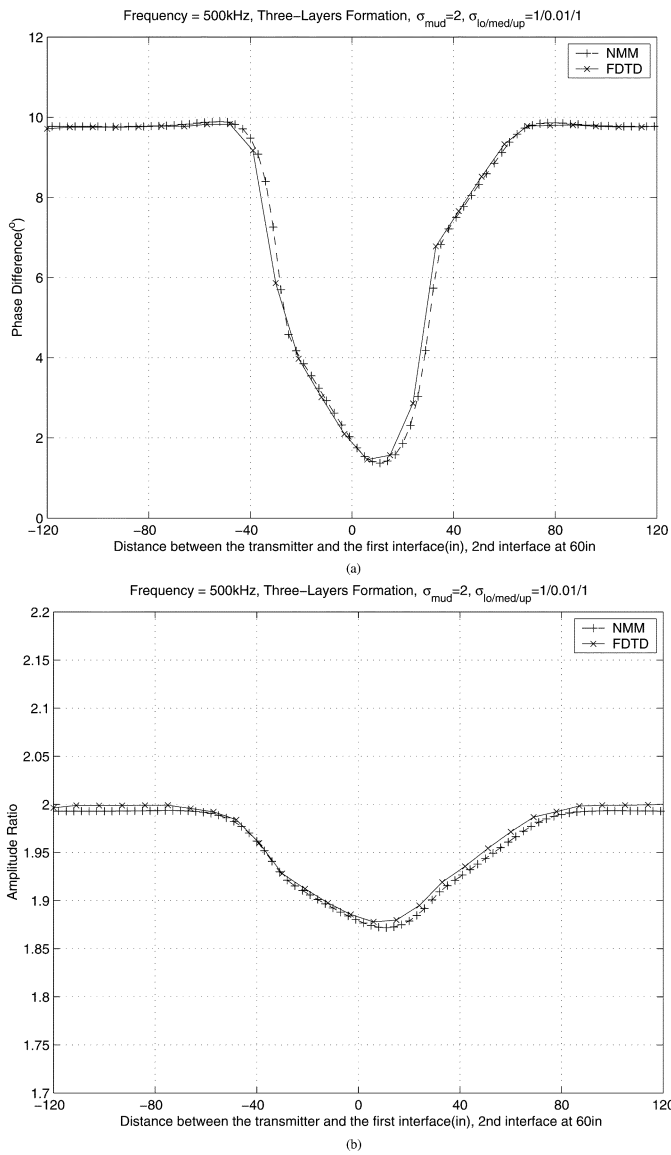


Fig. 16. FDTD and NMM results of a 500-kHz LWD tool response in a three-layer formation with lower, middle, and upper layer conductivities equal to 1, 0.01, and 1 mho/m, respectively. The conductivity of the mud is 2 mho/m. The middle bed is 60 in thick.

TABLE I

PHASE VELOCITY, WAVELENGTH, TIMESTEP, AND NORMALIZED CPU TIME WITH SCALED PERMITTIVITIES

ϵ_r	$\sigma/\omega\epsilon$	$v(x10^6)$ [m/s]	λ [m]	Δt [ps]	normalized CPU time
1	1797.5	299.79	2997.9	13.03	1.000
17.975	100	70.71	707.10	55.24	0.336
179.75	10	22.36	233.60	174.69	0.139

The use of PML as absorbing boundary condition for the cylindrical FDTD algorithms allows the use of more compact grids around the logging tool, and the use of locally conformal FDTD techniques reduces the staircasing error present in the representation of the borehole wall for eccentric problems. Finally, for tools operating at lower frequencies, the use of permittivity scaling has shown to be useful in reducing the computation time for diffusive problems. For example, the CPU time necessary to run a 100 KHz LWD tool after scaling is about 13% of the original CPU time (with the actual permittivity) for the case considered in Table I.

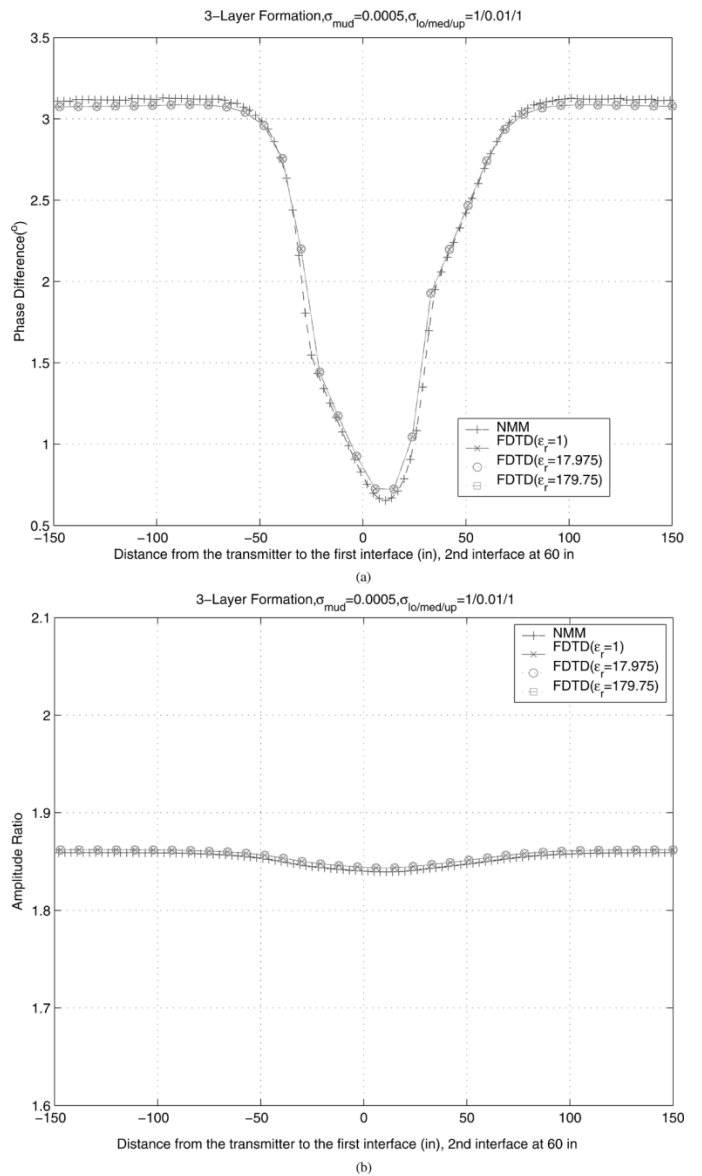


Fig. 17. FDTD and NMM results of a 500-kHz LWD tool response in a three-layer formation with lower, middle, and upper layer conductivities again equal to 1, 0.01, and 1 mho/m, respectively. The mud conductivity is now 0.0005 mho/m. The middle bed is 60 in thick.

ACKNOWLEDGMENT

The authors would like to thank the reviewers for their useful suggestions.

REFERENCES

- [1] Z.-Q. Zhang and Q.-H. Liu, "Applications of the BCGS-FFT method to 3-D induction well-logging problems," *IEEE Trans. Geosci. Remote Sens.*, vol. 41, no. 5, pp. 998-1004, May 2003.
- [2] S. Liu and M. Sato, "Electromagnetic logging technique based on borehole radar," *IEEE Trans. Geosci. Remote Sens.*, vol. 40, no. 9, pp. 2083-2092, Sep. 2002.
- [3] J. Li and C. Liu, "A three-dimensional transmission line matrix (TLM) method for simulations of logging tools," *IEEE Trans. Geosci. Remote Sens.*, vol. 38, no. 4, pp. 1522-1529, Jul. 2000.
- [4] B. Anderson, "Simulation of induction logging by the finite-element method," *Geophysics*, vol. 49, no. 11, pp. 1943-1958, Nov. 1984.
- [5] T. Wang, S. Fang, and A. G. Mezzatesta, "Three-dimensional finite-difference resistivity modeling using an upgridding method," *IEEE Trans. Geosci. Remote Sens.*, vol. 38, no. 4, pp. 1544-1550, Jul. 2000.

- [6] Q. H. Liu, W. C. Chew, M. R. Taherian, and K. A. Safinya, "A modeling study of electromagnetic propagation tool in complicated borehole environments," *Log Anal.*, vol. 30, pp. 424–436, 1989.
- [7] Z. Q. Zhang and Q.-H. Liu, "Simulation of induction logging response using conjugate gradient method with nonuniform fast Fourier and fast Hankel transforms," *Radio Sci.*, vol. 36, no. 4, pp. 599–608, 2001.
- [8] J.-Q. He and Q.-H. Liu, "A nonuniform cylindrical FDTD with improved PML and quasi-PML absorbing boundary conditions," *IEEE Trans. Geosci. Remote Sens.*, vol. 37, no. 2, pp. 1066–1072, Mar. 1999.
- [9] F. L. Teixeira and W. C. Chew, "Finite-difference computation of transient electromagnetic waves for cylindrical geometries in complex media," *IEEE Trans. Geosci. Remote Sens.*, vol. 38, no. 4, pp. 1530–1543, Jul. 2000.
- [10] J. Berenger, "Three-dimensional perfectly matched layer for the absorption of electromagnetic waves," *J. Comput. Phys.*, vol. 127, no. 2, pp. 363–379, 1996.
- [11] F. L. Teixeira and W. C. Chew, "PML-FDTD in cylindrical and spherical grids," *IEEE Microw. Guided Wave Lett.*, vol. 7, pp. 285–287, Sep. 1997.
- [12] J. R. Lovell and W. C. Chew, "Effect of tool eccentricity on some electrical well-logging tools," *IEEE Trans. Geosci. Remote Sens.*, vol. 28, no. 1, pp. 127–136, Jan. 1990.
- [13] W. Yu and R. Mittra, "A conformal finite difference time domain technique for modeling curved dielectric surface," *IEEE Microw. Wireless Compon. Lett.*, vol. 11, pp. 25–27, Jan. 2001.
- [14] C. M. Furse, "Faster than Fourier: Ultra-efficient time to frequency-domain conversions for FDTD simulations," *IEEE Antennas Propag. Mag.*, vol. 42, pp. 24–34, Dec. 2000.
- [15] C. M. Furse, D. H. Roper, D. N. Buechler, D. A. Christensen, and C. H. Durney, "The problem and treatment of DC offsets in FDTD simulations," *IEEE Antennas Propag. Mag.*, vol. 48, no. 8, pp. 1198–1201, Aug. 2000.
- [16] A. Taflov and S. Hagness, *Computational Electrodynamics: The Finite-Difference Time-Domain Method*, 2nd ed. Norwood, MA: Artech House, 2000.
- [17] R. Holland, "Finite-difference time-domain (FDTD) analysis of magnetic diffusion," *IEEE Trans. Electromagn. Compat.*, vol. 36, no. 1, pp. 32–39, Feb. 1994.
- [18] T. Wang and G. W. Hohmann, "A finite difference, time-domain solution for three-dimensional electromagnetic modeling," *Geophysics*, vol. 58, pp. 797–809, 1993.
- [19] R. H. Hardman and L. C. Shen, "Charts for correcting effects of formation dip and hole deviation on induction logs," *Log Anal.*, vol. 4, no. 28, pp. 349–356, Jul.–Aug. 1987.
- [20] R. Chemali, S. Gianzero, and S. M. Su, "The dual laterolog in common complex situations," in *Proc. 29th Annu. Logging Symp. Transactions: Soc. Professional Well Log Analysts*, vol. 1, 1988, pp. 1–25.

Yik-Kiong Hue was born in Kuala Lumpur, Malaysia, in 1977. He received the B.S. and M.S. degrees in electrical engineering from The Ohio State University, Columbus, in 2001 and 2003, respectively. He is currently pursuing the Ph.D. degree at The Ohio State University.

He is currently with the ElectroScience Laboratory, Department of Electrical Engineering and Computer Engineering, The Ohio State University. His current research interest includes numerical modeling for geophysical application. Mr. Hue was the recipient of a 2004-05 SPWLA scholarship.

Fernando L. Teixeira (S'96–M'99–SM'03) received the Ph.D. degree in electrical engineering from the University of Illinois, Urbana-Champaign, in 1999.

From 1996 to 1999, he was a Research Assistant with the University of Illinois. From 1999 to 2000, he was a Postdoctoral Research Associate with the Research Laboratory of Electronics, Massachusetts Institute of Technology, Cambridge, MA. Since 2000, he has been an Assistant Professor with the Department of Electrical and Computer Engineering, The Ohio State University (OSU), Columbus, OH. He has edited one book and has published over 50 journals articles and book chapters.

Dr. Teixeira received the IEEE MTT Fellowship Award in 1998, the Raj Mittra Outstanding Research Award from the University of Illinois in 1999, a URSI Young Scientist Award in 2002, a National Science Foundation CAREER Award in 2004, and the OSU Lumley Research Award in 2004. He is a member of Sigma Xi, Phi Kappa Phi, and Elected Member of U.S. Commission B of URSI.

Luis San Martin received the Ph.D. degree in physics from the University of Illinois, Urbana-Champaign, in 1998.

He is a Principal Scientist with the Sensor Physics Department, Halliburton Energy Services, Houston, TX. After graduation, he joined Halliburton Energy Services Research. He is currently with the Sensor Physics Group as part of the Electromagnetic Group.

Michael S. Bittar received the B.S., M.S., and Ph.D. degrees in electrical engineering from the University of Houston, Houston, TX, in 1983, 1986, and 1990, respectively.

He is the Resistivity Team Leader and the Sensor Physics Manager for both Sperry–Sun and Logging & Perforating of Halliburton Energy Services, Houston. He joined Sperry–Sun in 1990 and has been working on electrical resistivity tools design and theoretical modeling of electromagnetic wave tools. From 1984 to 1990, he was a Research Assistant in the Well-Logging Laboratory, University of Houston. He holds many U.S. and international patents and is the author of various publications on electromagnetic logging.